



Lagrangian Stochastic Modeling of Stratified Atmospheric Boundary Layer

Jihoon Shin¹ · Jong-Jin Baik²

Received: 19 July 2023 / Accepted: 15 November 2023
© The Author(s) 2024

Abstract

A single-column turbulence model for stratified atmospheric boundary layer (ABL), which solves the transport equations of turbulence probability density function (PDF) using a Lagrangian stochastic modeling (LSM) approach, is proposed in this study. This study adopts previously developed stochastic differential equations (SDEs) for particle velocity and temperature and extends the LSM to simulate inhomogeneous turbulence. The proposed LSM is tested for its ability to fully simulate statistics of inhomogeneous stratified turbulence. In the model, particles evolve by SDEs, and turbulence statistics are calculated by averaging the properties of particles. The model provides a full representation of turbulence PDF and simulates turbulent transport without any modeling assumption. The model performance is evaluated against large-eddy simulation (LES) results in the simulations of convective and stable ABL cases. For the convective ABL, LSM realistically simulates the entrainment process with the temperature and heat flux profiles that closely match with LES. The joint PDF simulated by LSM reproduces a curved and highly skewed shape, and some distinct features, like the asymmetric distribution of vertical velocity and the separation of the PDF in the entrainment zone, are simulated. LSM also reproduces the entrainment enhancement by wind shear in the simulation of sheared convective ABL. The LSM simulation of stable ABL predicts realistic turbulence intensity and mean field profiles, where Gaussian-like PDFs are simulated both in LSM and LES.

Keywords Atmospheric boundary layer · Lagrangian stochastic modeling · Stratified turbulence

1 Introduction

The Reynolds stress and scalar flux equations emerge when the Navier–Stokes and scalar conservation equations are Reynolds-averaged, respectively, and are the complete set of equations that model the time evolutions of turbulent fluxes. The second-moment closure (SMC)

✉ Jong-Jin Baik
jjbaik@snu.ac.kr

¹ Department of Environmental Atmospheric Sciences, Pukyong National University, Busan, South Korea

² School of Earth and Environmental Sciences, Seoul National University, Seoul, South Korea

and higher-order closure models are designed to close the unknown terms in the Reynolds stress and scalar flux equations. The moment closure assumption is unavoidable because, in any n -th order moment transport equation, there are higher order terms in the equation. The number of prognostic equations and unknowns rapidly increases as the order of moment increases. To limit the number of equations and unknowns, SMC and higher-order closure models solve prognostic equations only for the first several orders of moments (typically up to third moments), and higher-order moments are closed by appropriate assumptions. The moment closure limits the probability density function (PDF) of turbulence to be represented by several orders of moments.

In the atmospheric modeling community, there is an emerging need for PDF-based sub-grid turbulence models capable of simulating non-local turbulent transport and various types of clouds when coupled with microphysics. For instance, stratus-type clouds can be represented by a PDF in which a large fraction is saturated and has a small vertical velocity, and cumulus-type clouds can be represented by a PDF in which a small fraction is saturated and has a large vertical velocity. This category of models has the potential to be used as unified parameterizations of the boundary layer and moist convection. A widely-used application for numerical atmospheric models is the assumed PDF higher-order turbulence closures. The method assumes a functional form of PDF, and the parameters of the PDF are diagnosed using prognosed turbulent moments. The Cloud Layers Unified By Binormals (CLUBB; Golaz et al. 2002; Bogenschutz et al. 2013), which assumes a double Gaussian PDF, has been implemented in Community Atmospheric Model version 6 (CAM6) and shows improvement in the simulation of boundary layer clouds (Danabasoglu et al. 2020; Li et al. 2022). The double Gaussian PDF well represents the observed PDF of boundary layer turbulence and clouds in many cases (Bogenschutz et al. 2010). However, the assumed PDFs have fundamental limitations in that they can not represent more complex distribution, like when strong convective downdrafts exist (Fitch 2019). Reconstructing an arbitrary distribution from a finite number of its moments is an ill-posed inverse problem from a mathematical viewpoint (Schmüdgen 2017). Therefore, getting the correct PDF from higher-order turbulence closures is not possible.

The most comprehensive methods to model turbulence are so-called “PDF methods” that directly solve a transport equation for a joint PDF (Pope 2000). The exact transport equation for PDF can be derived from the Navier–Stokes equation, but it contains unclosed terms related to fluctuating pressure and viscosity. The transport equation for PDF is typically modeled and numerically solved using the generalized Langevin equation (Pope 1983). The Langevin equation is a stochastic differential equation (SDE) that describes the Lagrangian motion of a particle in turbulent flows. The PDF transport equation is essentially the Fokker–Planck equation corresponding to the Langevin equation. In addition, Pope (1994) demonstrated that the second moment of the Langevin equation is the Reynolds stress closure. On this basis, PDF methods have been widely adopted in engineering applications of complex turbulent flows like combustion and reactive flows. The joint PDFs of these applications are high dimensional (velocity, dissipation, and chemical components), so Monte Carlo techniques have been employed where an ensemble of Lagrangian particles represents the PDF. Therefore, PDF methods are mostly developed in the form of Lagrangian stochastic modeling (LSM) of turbulence.

In the atmospheric modeling community, LSM is commonly used to model passive scalar dispersion (e.g., air pollutants) rather than to model turbulence. Historically, the Lagrangian stochastic model was originally introduced by Taylor (1922) to model atmospheric dispersion. Since then, much effort has been made to simulate turbulence statistics of complex flows using LSM approaches. Thomson (1987) investigated necessary criteria for LSMs to simulate the

statistics of inhomogeneous or unsteady turbulence correctly. After Pope (1994) demonstrated that any generalized Langevin equation corresponds to a unique Reynolds stress model, LSMs have been developed into PDF methods to fully compute the statistics of inhomogeneous turbulence. It is natural to extend PDF methods to stratified turbulence, which will be useful for PDF modeling of the atmospheric boundary layer (ABL). A number of studies have proposed LSMs to model atmospheric dispersion in stratified conditions (Pearson et al. 1983; Venkatram et al. 1984; Heinz 1997; Das and Durbin 2005). However, using LSMs as PDF methods for stratified flows is an area that requires further research. Throughout this paper, LSM refers to the LSM specifically being used as a PDF method.

Despite the relatively higher computational cost, testing the LSM approach for atmospheric turbulent flows is important in the process of developing PDF-based subgrid turbulence models. In LSM, convection is represented exactly without modeling assumptions, so the turbulence modeling problem reduces to modeling fluctuating pressure and dissipation. As higher-order closure models and assumed-PDF methods give an incomplete representation of PDF, LSM can be served as a reference model; the joint PDF simulated from LSM can be used to evaluate statistical moments calculated from SMC models.

This study implements LSM as a single-column turbulence model and tests its performance in simulating stratified ABL. We adopt the LSM equations for stratified flows proposed by Das and Durbin (2005), which exactly reproduce SMC equations that have been widely used to model stratified ABL. Das and Durbin (2005) tested their LSM to simulate dispersion in homogenous turbulence, where Reynolds stresses, heat flux, and dissipation are computed from an SMC model. This study extends the LSM of Das and Durbin (2005) to simulate inhomogeneous stratified turbulence by including pressure transport and the stochastic dissipation model designed for inhomogeneous turbulence. Also, we test an application of the LSM as a PDF method for ABL modeling. For this purpose, we adopt some techniques from several PDF-solving algorithms for turbulence (Muradoglu et al. 2001; Jenny et al. 2001; Wild 2013), extend them to simulate stratified turbulence, and propose a PDF-solving algorithm that is appropriate for atmospheric applications. The model is tested for three idealized cases: the Dry Convective Boundary Layer (DCBL), DCBL with shear (DCBL-S), and the first Global Energy and Watercycle Experiment (GEWEX) Atmospheric Boundary Layer Study (GABLS1) cases. The various statistics from the model are compared with large-eddy simulation (LES) results. We also discuss the future extension of the model to improve model performance, reduce computational cost, and simulate clouds.

2 Turbulence Model Equations

2.1 Second-Moment Closure Corresponding to Lagrangian Stochastic Model

The Reynolds stress and heat flux equations with the anelastic approximation are read as:

$$\frac{Du'_i u'_j}{Dt} = T_{ij}^t + T_{ij}^p + \Pi_{ij} + \mathcal{P}_{ij} + \mathcal{G}_{ij} - \epsilon_{ij}, \quad (1)$$

$$\frac{Du'_i \theta'}{Dt} = T_{\theta i}^t + T_{\theta i}^p + \Pi_{\theta i} + \mathcal{P}_{\theta i} + \mathcal{G}_{\theta i} - \epsilon_{\theta i}, \quad (2)$$

respectively, where $D/Dt \equiv \partial/\partial t + \overline{u_k} \partial/\partial x_k$ is the material derivative, and the other terms are defined as:

$$\begin{aligned}
T_{ij}^t &\equiv -\overline{\frac{\partial u'_i u'_j u'_k}{\partial x_k}}, & T_{\theta i}^t &\equiv -\overline{\frac{\partial u'_i \theta' u'_k}{\partial x_k}} \\
T_{ij}^p &\equiv -\frac{1}{\rho_0} \overline{\frac{\partial u'_i p'}{\partial x_j}} - \frac{1}{\rho_0} \overline{\frac{\partial u'_j p'}{\partial x_i}}, & T_{\theta i}^p &\equiv -\frac{1}{\rho_0} \overline{\frac{\partial \theta' p'}{\partial x_k}} \\
\Pi_{ij} &\equiv \frac{p'}{\rho_0} \left(\overline{\frac{\partial u'_i}{\partial x_j}} + \overline{\frac{\partial u'_j}{\partial x_i}} \right), & \Pi_{\theta i} &\equiv \frac{p'}{\rho_0} \overline{\frac{\partial \theta'}{\partial x_i}} \\
\mathcal{P}_{ij} &\equiv -\overline{u'_i u'_k} \frac{\partial \overline{u_j}}{\partial x_k} - \overline{u'_j u'_k} \frac{\partial \overline{u_i}}{\partial x_k}, & \mathcal{P}_{\theta i} &\equiv -\overline{u'_i u'_k} \frac{\partial \overline{\theta}}{\partial x_k} - \overline{u'_k \theta'} \frac{\partial \overline{u_i}}{\partial x_k} \\
\mathcal{G}_{ij} &\equiv -\frac{1}{\theta_0} \left(\overline{g_i u'_j \theta'} + \overline{g_j u'_i \theta'} \right), & \mathcal{G}_{\theta i} &\equiv -\frac{g_i}{\theta_0} \overline{\theta'^2} \\
\epsilon_{ij} &\equiv 2\nu \overline{\left(\frac{\partial u'_i}{\partial x_k} \frac{\partial u'_j}{\partial x_k} \right)}, & \epsilon_{\theta i} &\equiv (\lambda + \nu) \overline{\left(\frac{\partial u'_i}{\partial x_k} \frac{\partial \theta'}{\partial x_k} \right)}
\end{aligned} \tag{3}$$

and represent (from top to bottom) the turbulent transport, pressure transport, pressure–rate-of-strain correlation, shear (or mean-field) production, buoyancy production, and dissipation tensors. $u_i = \{u, v, w\} = \overline{u_i} + u'_i$ is the velocity component, $\theta = \overline{\theta} + \theta'$ is the potential temperature, and $p = \overline{p} + p'$ is the pressure, where they are decomposed into the mean and perturbation components by Reynolds averaging. g_i is the component of gravitational acceleration, ν is the kinematic viscosity, λ is the thermal diffusivity, and ρ_0 and θ_0 are the basic state density and potential temperature, respectively, which are only functions of z .

The equations for turbulent kinetic energy (TKE) (essentially half the trace of (1)), $k = \frac{1}{2} \overline{u'_k{}^2}$, and half potential temperature variance are written as:

$$\frac{Dk}{Dt} = T^t + T^p + \mathcal{P} + \mathcal{G} - \epsilon, \tag{4}$$

$$\frac{1}{2} \frac{D\overline{\theta'^2}}{Dt} = T_\theta^t + \mathcal{P}_\theta - \epsilon_\theta, \tag{5}$$

respectively, where the terms in (4) are half the trace of the terms in (1) and $T_\theta^t = -\overline{\partial u'_k \theta'^2 / \partial x_k}$, $\mathcal{P}_\theta = -\overline{u'_k \theta' \partial \overline{\theta} / \partial x_k}$, and $\epsilon_\theta = \lambda (\partial \theta' / \partial x_k)^2$ are the turbulent transport, production, and dissipation of half temperature variance, respectively.

The LSM formulation of Das and Durbin (2005) is based on the general linear formation of SMC. This SMC formulation is widely used for modeling the stratified ABL. The dissipation anisotropy is neglected ($\epsilon_{ij} \approx (2/3)\epsilon\delta_{ij}$) with an assumption of local isotropy at high Reynolds numbers, and the pressure–rate-of-strain (also known as pressure redistribution) is modeled with the standard isotropization of production from Launder et al. (1975). The SMC formulation is:

$$\begin{aligned}
\frac{D\overline{u'_i u'_j}}{Dt} &= T_{ij}^t + T_{ij}^p \\
&\quad - c_1 \frac{\epsilon}{k} \left(\overline{u'_i u'_j} - \frac{2}{3} k \delta_{ij} \right) - c_2 \left(\mathcal{P}_{ij} - \frac{2}{3} \mathcal{P} \delta_{ij} \right) \\
&\quad - c_3 \left(\mathcal{D}_{ij} - \frac{2}{3} \mathcal{P} \delta_{ij} \right) - c_s k \mathcal{S}_{ij} - c_5 \left(\mathcal{G}_{ij} - \frac{2}{3} \mathcal{G} \delta_{ij} \right) \\
&\quad + \mathcal{P}_{ij} + \mathcal{G}_{ij} - \frac{2}{3} \epsilon \delta_{ij},
\end{aligned} \tag{6}$$

$$\begin{aligned} \frac{Du'_i\theta'}{Dt} &= T_{\theta i}^t + T_{\theta i}^p \\ &\quad - c_{1\theta} \frac{\epsilon}{k} \overline{u'_i\theta'} - (1 - c_{2\theta}) \overline{u'_k\theta'} \frac{\partial \overline{u_i}}{\partial x_k} + c_{3\theta} \overline{u'_k\theta'} \frac{\partial \overline{u_k}}{\partial x_i} \\ &\quad - (1 - c_{4\theta}) \overline{u'_i u'_k} \frac{\partial \overline{\theta}}{\partial x_k} - (1 - c_{5\theta}) \frac{g_i}{\theta_0} \overline{\theta'^2}, \end{aligned} \quad (7)$$

$$\frac{1}{2} \frac{D\overline{\theta'^2}}{Dt} = T_{\theta}^t - \overline{u'_k\theta'} \frac{\partial \overline{\theta}}{\partial x_k} - \frac{\mathcal{R}}{2} \frac{\epsilon \overline{\theta'^2}}{k}, \quad (8)$$

where $S_{ij} = (1/2)(\partial \overline{u_i}/\partial x_j + \partial \overline{u_j}/\partial x_i)$, $\mathcal{D}_{ij} = -\overline{u'_i u'_k} \partial \overline{u_k}/\partial x_j - \overline{u'_j u'_k} \partial \overline{u_k}/\partial x_i$, δ_{ij} is the Kronecker delta, and $c_1, c_2, c_3, c_5, c_{1\theta}, c_{2\theta}, c_{3\theta}, c_{4\theta}, c_{5\theta}, c_s$ and \mathcal{R} are constants.

2.2 Lagrangian Stochastic Model

2.2.1 Stochastic Differential Equations for Velocity and Scalar

Das and Durbin (2005) derived LSM equations corresponding to the above SMC formulation. We choose a simplified form of LSM which can be derived if the values of $c_{2\theta}$, $c_{3\theta}$, and $c_{5\theta}$ are equal to c_2 , c_3 , and c_5 , respectively, and $c_s = 0$. The LSM for a general case is also available, but the formulation is more complicated. The simplified form of LSM is just a special case of the general form, where both forms reproduce the above SMC formulation. The simplified form of LSM is:

$$dx_i = u_i dt, \quad (9)$$

$$\begin{aligned} du_i &= -\frac{c_1}{2} \frac{\epsilon}{k} u'_i dt + c_{2\theta} u'_k \frac{\partial \overline{u_i}}{\partial x_k} dt + c_{3\theta} u'_k \frac{\partial \overline{u_k}}{\partial x_i} dt \\ &\quad - (1 - c_{5\theta}) \frac{g_i}{\theta_0} \theta' dt + \underbrace{C_{pt} \left(\frac{u'_k u'_k}{2k} - 1 \right) \frac{\partial k}{\partial x_i} dt}_{\text{pressure transport}} + \sqrt{c_0 \epsilon} dW_i, \end{aligned} \quad (10)$$

$$d\theta = -\left(c_{1\theta} - \frac{c_1}{2}\right) \frac{\epsilon}{k} \theta' dt + c_{4\theta} u'_k \frac{\partial \overline{\theta}}{\partial x_k} dt + \sqrt{c_{\theta} \epsilon} dW_{\theta}. \quad (11)$$

Here, dW is the increment of Wiener process and ϵ is the Reynolds-averaged dissipation rate. The coefficients c_0 and c_{θ} are specified as:

$$\begin{aligned} c_0 &= \frac{2}{3} \left[c_1 - 1 + (c_2 + c_3) \frac{\mathcal{P}}{\epsilon} + c_5 \frac{\mathcal{G}}{\epsilon} \right], \\ c_{\theta} &= -2c_{4\theta} \overline{u'_k \theta'} \frac{\partial \overline{\theta}}{\partial x_k} + \frac{\epsilon}{k} (2c_{1\theta} - c_1 - \mathcal{R}) \overline{\theta'^2}. \end{aligned} \quad (12)$$

In order to satisfy the realizability condition that c_0 and c_{θ} are non-negative, c_1 and $c_{1\theta}$ are replaced by:

$$\begin{aligned} c_{1,\text{new}} &= \max \left[c_1, 1 - (c_2 + c_3) \frac{\mathcal{P}}{\epsilon} - c_5 \frac{\mathcal{G}}{\epsilon} \right], \\ c_{1\theta,\text{new}} &= \max \left[c_{1\theta}, 0.5 \left[2 \frac{k}{\epsilon \theta'^2} c_{4\theta} \overline{u'_k \theta'} \frac{\partial \overline{\theta}}{\partial x_k} + (c_{1,\text{new}} + \mathcal{R}) \right] \right]. \end{aligned} \quad (13)$$

The standard model constants for LSM are listed in Table 1. Using the simplified form of LSM constrains the choice of the values of constants. However, the constants are calibrated using a bunch of experimental and numerical data in Das and Durbin (2005), and the calibrated model has the correct critical Richardson number at approximately 0.25, which justifies the use of the simplified form. $c_s = 0$ is used in the standard isotropization of production model. Note that different values for the constants have been used in the literature. In addition to the original LSM formulation, the pressure transport is parameterized following Van Slooten et al. (1998) with a model constant, C_{pt} (default value: 0.2). The pressure transport is modeled as an additional force exerted on high-energy particles towards a kinetic energy gradient. The pressure transport is neglected or jointly modeled with turbulent transport in SMC models. Das and Durbin (2005) did not include any pressure transport parameterization as they tested their model for homogeneous turbulence.

2.2.2 Stochastic Differential Equation for Dissipation

Information on the dissipation is required to close the LSM formulation. In most atmospheric turbulence models, the turbulent length scale is modeled algebraically to calculate eddy viscosity or dissipation. In this study, the SDE for dissipation is adopted from Van Slooten et al. (1998), where the source of dissipation is modeled as the standard k - ϵ model. Compared to the standard k - ϵ model, the SDE has advantages in that inhomogeneity of dissipation is simulated in a natural fashion as every particle has its dissipation value. It is possible to compute dissipation using the standard k - ϵ model, but we adopt the SDE to fully accommodate the advantages of PDF methods. The SDE is expressed in terms of turbulence frequency, and the turbulence frequency is defined as a stochastic variable, $\omega = \epsilon^*/k$, where ϵ^* is the local dissipation rate. Here, the asterisk indicates the local value (value of each particle) to distinguish it from the Reynolds-averaged value ϵ . Therefore, $\epsilon = \overline{\epsilon^*}$ holds. The SDE is constructed to model the intermittency of turbulence. Kolmogorov (1962) hypothesized that instantaneous dissipation is log-normally distributed at high Reynolds numbers. The stationary PDF from the SDE is a gamma distribution, which is similar to a log-normal distribution. The SDE also treats the entrainment of nonturbulent fluid. The model equation from Van Slooten et al. (1998) is:

$$d\omega = -C_3(\omega - \overline{\omega})\Omega dt - \Omega\omega S_\omega dt + \sqrt{2C_3C_4\overline{\omega}\Omega} dW, \quad (14)$$

where $\Omega \equiv C_\Omega \langle \omega \mid \omega \geq \overline{\omega} \rangle$ ($C_\Omega \approx 0.6893$) is the conditional-mean turbulence frequency, C_3 and C_4 are constants, and the (negative) source of turbulence frequency, which is related to the k - ϵ model, is:

$$S_\omega = (C_{\epsilon 2} - 1) - (C_{\epsilon 1} - 1)\frac{\mathcal{P}}{\epsilon} - (C_{\epsilon 3} - 1)\frac{G}{\epsilon}, \quad (15)$$

where $C_{\epsilon 1}$, $C_{\epsilon 2}$, and $C_{\epsilon 3}$ are model parameters. $C_{\epsilon 1} = 1.44$ is the commonly used value, and different values for $C_{\epsilon 2}$ and $C_{\epsilon 3}$ are proposed in studies of stratified turbulence (Pereira and Rocha 2010; Goudsmit et al. 2002; Venayagamoorthy et al. 2003; Želi et al. 2020). In this study, $C_{\epsilon 2} = 1.82$ and $C_{\epsilon 3} = 0$ are chosen following Želi et al. (2020). The value of $C_{\epsilon 3}$ exhibits large uncertainty depending on flow regime (Venayagamoorthy et al. 2003), so further investigation is required to parameterize the buoyancy effect on dissipation rate.

Following Van Slooten et al. (1998), the mean time scale of turbulence (ϵ/k) in LSM is specified using the conditional-mean turbulence frequency Ω rather than $\overline{\omega}$, in the sense that

Table 1 Standard model constants

Constant	Value	Constant	Value
c_1	1.8	$c_{1\theta}$	2.5
c_2	0.6	$c_{2\theta}$	0.6
c_3	0.0	$c_{3\theta}$	0.0
c_5	1/3	$c_{4\theta}$	0.0
\mathcal{R}	1.5	$c_{5\theta}$	1/3
$C_{\epsilon 1}$	1.44	C_3	1.0
$C_{\epsilon 2}$	1.82	C_4	0.25
$C_{\epsilon 3}$	0.0	C_{pt}	0.2

the turbulence time scale is mainly determined by turbulent region. Therefore, the Reynolds-averaged dissipation is computed as:

$$\epsilon = \Omega k. \quad (16)$$

Van Slooten et al. (1998) demonstrated that using Ω as turbulence time scale instead of $\bar{\omega}$ substantially improves their model performance.

3 Numerical Implementation

This section explains detailed numerical methods to implement LSM as a single-column turbulence model: how the particles evolve in a model grid and how the turbulence statistics are calculated from the particles. In this study, a particle-in-cell method, which is greatly motivated by the work of Jenny et al. (2001), is adopted to get the turbulence statistics from the particles.

3.1 Overview

Figure 1a summarizes the algorithm of the single-column turbulence model. At each time step, particle properties and positions are advanced with the LSM equations, and an appropriate boundary condition is applied to the particles. The vertical turbulent fluxes ($\overline{w'u'_i}$ and $\overline{w'\theta'}$) are calculated by averaging particle properties onto a vertical model grid. Then, the time evolutions of mean fields ($\overline{u_i}$ and $\overline{\theta}$) are calculated as the convergence of the turbulent fluxes. This approach (predicting turbulent fluxes) is consistent with other atmospheric turbulence models in which the transports of mean fields are simulated by a host dynamic model.

A one-dimensional vertical grid is considered, where z_k ($k = \{1, \dots, N_z\}$) represents the height of grid midpoints and $z_{k+\frac{1}{2}}$ ($k = \{0, \dots, N_z\}$) represents the height of grid interfaces (N_z is the number of grid cells). A staggered grid configuration is adopted, where the mean fields ($\overline{u_i}$ and $\overline{\theta}$) are located at grid midpoints and the vertical fluxes ($\overline{w'u'_i}$ and $\overline{w'\theta'}$) are located at grid interfaces. Other turbulence statistics (k , $\bar{\omega}$, Ω , \mathcal{P} , and \mathcal{G}) are assumed to be located at grid midpoints (Fig. 1b).

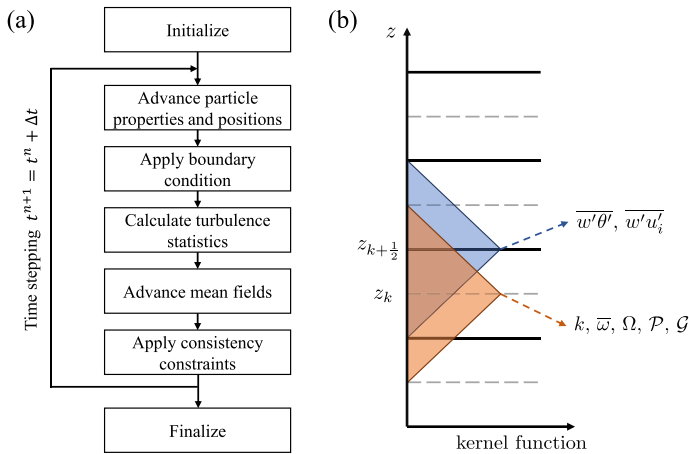


Fig. 1 **a** Schematic of the algorithm of the single-column Lagrangian stochastic turbulence model. **b** Schematic of the vertical grid system and kernel functions

3.2 Numerical Integration of Particles

The particle properties and positions are advanced by numerically integrating the LSM equations, where horizontal derivatives in the LSM equations are neglected following the single-column model framework. The numerical integration method used in this study is adopted from Jenny et al. (2001). The particle position is integrated using a mid-point rule to achieve second-order accuracy. In the first half step, the particle is moved to:

$$z^{*n+\frac{1}{2}} = z^{*n} + \frac{\Delta t}{2} w^{*n}, \quad (17)$$

where superscript n denotes the old time level and $n+1$ is the new time level. Then, u_i^{*n+1} , θ^{*n+1} , and ω^{*n+1} are obtained with the coefficient evaluated at $z^{*n+(1/2)}$. The particle position at the new time level is:

$$z^{*n+1} = z^{*n} + \frac{\Delta t}{2} (w^{*n} + w^{*n+1}). \quad (18)$$

The SDE for velocity (10) can be written as:

$$du_i^*(t) = a_i dt + b_{ij} u_j^* dt + c_i^{1/2} dW_i. \quad (19)$$

A second-order scheme is used to integrate the Langevin equation:

$$\begin{aligned} \Delta u_i^* &= \left(a_i + b_{ij} u_j^{*n} \right) \Delta t + (c_i \Delta t)^{1/2} \xi_i, \\ u_i^{*n+1} &= u_i^{*n} + \Delta u_i^* + \frac{1}{2} b_{ij} \Delta u_j^* \Delta t, \end{aligned} \quad (20)$$

where ξ is a random variable with standard normal distribution. The SDE for potential temperature (11) is integrated with the same scheme.

The SDE for turbulence frequency (14) can be rewritten as:

$$d\omega^* = A dt - B \omega^* dt + (C \omega^*)^{1/2} dW, \quad (21)$$

where $A = C_3 \bar{\omega} \Omega$, $B = (C_3 + S_\omega) \Omega$, and $C = 2C_3 C_4 \bar{\omega} \Omega$. The time integration can be done analytically assuming A , B , and C are invariant for a single time step:

$$\begin{aligned} X &= \omega^{*n} e^{-B\Delta t} + \frac{A}{B} (1 - e^{-B\Delta t}), \\ \sigma^2 &= \frac{C\Delta t}{2(1 + B\Delta t)} (X + \omega^{*n}), \\ \omega^{n+1} &= \max(0, X + \sigma\xi). \end{aligned} \quad (22)$$

3.3 Boundary Condition

A simple reflective boundary condition is imposed for the upper boundary. For a lower boundary, an appropriate boundary condition needs to be imposed on the particles so that the particle properties are modified by surface momentum and heat fluxes. We adopted the wall function for particle methods suggested by Dreeben and Pope (1997). The particles are reflected at the specified height z_s in the log-law region so that the model equations do not need to be solved below z_s . In our model, z_s is set as the height of the midpoint of the lowest model layer. The reflected particle properties are specified as:

$$w_R^* = -w_I^*, \quad (23)$$

$$u_R^* = u_I^* - \frac{2 \left(\overline{u'w'} \right)_s}{\left(\overline{w'^2} \right)_s} w_I^*, \quad (24)$$

$$v_R^* = v_I^* - \frac{2 \left(\overline{v'w'} \right)_s}{\left(\overline{w'^2} \right)_s} w_I^*, \quad (25)$$

$$\theta_R^* = \theta_I^* - \frac{2 \left(\overline{w'\theta'} \right)_s}{\left(\overline{w'^2} \right)_s} w_I^*, \quad (26)$$

where the subscript s denotes the value at z_s and the subscripts I and R are for incident and reflected, respectively. With the constant flux approximation in the surface layer, $(\overline{u'w'})_s$, $(\overline{v'w'})_s$, and $(\overline{w'\theta'})_s$ are specified as surface fluxes. $(\overline{w'^2})_s$ is specified as the vertical velocity variance in the lowest model layer.

Dreeben and Pope (1997) also proposed a wall function for turbulence frequency. However, the wall function is ill-defined when turbulence frequency near the wall is close to 0, so an alternate boundary condition is used for this study. The mean turbulence frequency at z_s is calculated with the approximation that TKE production and dissipation are balanced in the surface layer,

$$\epsilon_s \approx \mathcal{P}_s + \mathcal{G}_s = \frac{u_*^3}{\kappa z_s} + \frac{g}{\theta_0} \left(\overline{w'\theta'} \right)_s, \quad (27)$$

$$\bar{\omega}_s = \frac{\epsilon_s}{k_s}, \quad (28)$$

where κ is the von Karmann constant, u_* is the frictional velocity, and k_s is specified as k in the lowest model layer. Then, the reflected particles are randomly distributed with a gamma distribution in which the shape and scale parameters are $1/C_4$ and $C_4 \bar{\omega}_s$, respectively.

The surface momentum and heat fluxes need to be determined to evaluate (24)–(26) and (32). The surface fluxes can be either diagnosed from the similarity theory or specified as forcing. In this study, the surface fluxes are diagnosed with the particles in the lowest model layer with the Businger-Dyer similarity functions (Businger et al. 1971; Dyer 1974).

3.4 Calculation of Turbulence Statistics

Similar to Jenny et al. (2001), a linear kernel function, $\hat{g}(z)$, is used to estimate grid mean values from particles or interpolate grid mean values to particles. The kernel function can be located at either grid midpoints or interfaces, denoted as $\hat{g}_k(z)$ or $\hat{g}_{k+\frac{1}{2}}(z)$, respectively. The kernel function is defined as:

$$\hat{g}_k(z) = \begin{cases} (z_{k+1} - z)/(z_{k+1} - z_k) & z_{k+1} > z \geq z_k, \\ (z - z_{k-1})/(z_k - z_{k-1}) & z_k > z \geq z_{k-1}, \\ 0 & \text{otherwise.} \end{cases} \quad (29)$$

Figure 1b shows an example of the kernel functions. The statistics located at grid midpoints (interfaces) are calculated by averaging particles with $\hat{g}_k(z)$ ($\hat{g}_{k+\frac{1}{2}}(z)$) kernel. For example, $\overline{w'\theta'}$ is calculated as:

$$(\overline{w'\theta'})_{k+\frac{1}{2}} = \frac{\sum_{n=1}^{N_p} \left(\hat{g}_{k+\frac{1}{2}}(z^*) w'^* \theta'^* \right)_n}{\sum_{n=1}^{N_p} \left(\hat{g}_{k+\frac{1}{2}}(z^*) \right)_n}, \quad (30)$$

where the asterisk (*) denotes particle value, n is the particle index, and N_p is the total number of particles.

The interpolation of grid mean values to particle positions can also be done using the kernel functions. The weights for the interpolation are specified as $\hat{g}_k(z)$ or $\hat{g}_{k+\frac{1}{2}}(z)$. For example, $\bar{\theta}$ is interpolated to a particle position as:

$$\bar{\theta}^* = \hat{g}_k(z^*) \cdot (\bar{\theta})_k + \hat{g}_{k+1}(z^*) \cdot (\bar{\theta})_{k+1}, \quad (31)$$

when the particle is located between z_k and z_{k+1} . The interpolation is essentially a linear interpolation between the two grid mean values.

3.5 Time Evolutions of Mean Fields

The time evolutions of mean fields in our model are calculated as:

$$\begin{aligned} \frac{\partial \bar{u}}{\partial t} &= -\frac{1}{\rho_0} \frac{\partial \rho_0 \overline{u'w'}}{\partial z} - f(V_g - \bar{v}), \\ \frac{\partial \bar{v}}{\partial t} &= -\frac{1}{\rho_0} \frac{\partial \rho_0 \overline{v'w'}}{\partial z} + f(U_g - \bar{u}), \\ \frac{\partial \bar{\theta}}{\partial t} &= -\frac{1}{\rho_0} \frac{\partial \rho_0 \overline{w'\theta'}}{\partial z}, \end{aligned} \quad (32)$$

where f is the Coriolis parameter and U_g and V_g are the components of geostrophic wind in the x and y directions, respectively. Equation (32) is solved numerically using a combination of central differencing for spatial derivatives and forward differencing for time derivatives,

with a time step of Δt . The mean fields are calculated by (32) rather than averaging particle values because stochastic noise would violate the conservations of momentum and energy if particle-averaged values are used.

3.6 Consistency Constraints

As LSM uses a Monte Carlo approach to represent turbulence statistics, some evaluated statistics may have deviated from Eulerian statistics. Therefore, some numerical measures need to be taken to satisfy the consistency between them. The first requirement is that the mean fields calculated from (32) need to be consistent with the particle averaged values. To satisfy the requirement, the mean deviations ($\overline{u'^*}$, $\overline{v'^*}$, $\overline{w'^*}$, and $\overline{\theta'^*}$) are subtracted from every particle at each time step. The second requirement is that the particle density is consistent with the basic state density. Particles can be accumulated at certain positions (e.g., near the surface) due to numerical errors, and this is a common issue in other Lagrangian particle dispersion models. A particle density correction algorithm from Wild (2013) is adopted, as explained in Appendix 1.

4 Case Description and Model Setup

4.1 Case Description

The DCBL case is forced with a constant sensible heat flux of 0.1 K ms^{-1} and the initial potential temperature profile with a constant gradient of $\partial\bar{\theta}/\partial z = 3 \text{ K km}^{-1}$ and 300 K at the surface. The surface pressure, Coriolis parameter, and roughness length are set to 1015 hPa, 0 s^{-1} , and 0.01 m, respectively. We additionally test the DCBL case with wind shear (namely DCBL-S case) to test whether LSM simulates changes in the convective boundary layer by wind shear. The DCBL-S case is identical to the DCBL case, but a steady geostrophic wind profile of $(U_g, V_g) = (z/100, 0) \text{ m s}^{-1}$ is imposed, similar to the case of Conzemius and Fedorovich (2006). The initial wind profile is the same as the geostrophic wind profile. The DCBL and DCBL-S cases are integrated for 4 h.

The GABLS1 case setup is identical to Beare et al. (2006). This case is forced by a steady geostrophic wind profile of $(U_g, V_g) = (8, 0) \text{ m s}^{-1}$ and a time-varying surface temperature. The surface temperature is initialized as 265 K and decreases with a constant cooling rate of 0.25 K h^{-1} . The initial potential temperature profile is constant at 265 K from the surface up to 100 m and increases above it at a rate of 10 K km^{-1} . The initial wind profile is the same as the geostrophic wind profile. The surface pressure, Coriolis parameter, and roughness length are set to 1000 hPa, $1.39 \times 10^{-4} \text{ s}^{-1}$, and 0.1 m, respectively. The GABLS1 case is integrated for 9 h.

4.2 Large-Eddy Simulation and Lagrangian Stochastic Model Setup

The simulations with the University of California, Los Angeles large-eddy simulation (UCLA-LES) model (Stevens et al. 1999, 2005) are used to evaluate LSM. UCLA-LES solves a set of anelastic equations with the turbulence model of Smagorinsky–Lilly. The Smagorinsky coefficient and Prandtl number are set as 0.23 and 1/3, respectively. The LESs of the DCBL and DCBL-S cases are run with the domain size of $5.12 \times 5.12 \times 2 \text{ km}^3$ and the grid size of $20 \times 20 \times 20 \text{ m}^3$. To initialize turbulence, the simulations are initialized with

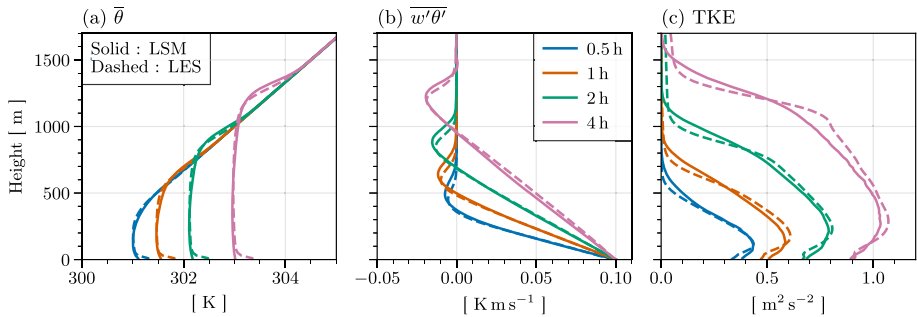


Fig. 2 Vertical profiles of **a** $\bar{\theta}$, **b** $\overline{w'\theta'}$, and **c** TKE in the simulations of the DCBL case from LSM (solid) and LES (dashed) at $t = 0.5, 1, 2$, and 4 h

random temperature perturbation of 0.2 K below 100 m height. The LES of GABLS1 case is run with the domain size of $400 \times 400 \times 400 \text{ m}^3$ and the grid size of $3.125 \times 3.125 \times 3.125 \text{ m}^3$, and initialized with random perturbation of 0.1 K below 50 m height. The model outputs are saved with an interval of 30 s for all cases.

The LSM simulations are conducted with the same vertical domain and vertical grid size as of LES. Also, the simulations are initialized with random temperature perturbations as done in LES so that turbulence is initialized in a consistent way. All cases are run with the total particle number of $N_p = 200000$. The fixed time step of $\Delta t = 5$ s is used for the DCBL and DCBL-S cases and $\Delta t = 2.5$ s for the GABLS1 case. The time step is determined to be less than the maximum time step required by CFL condition and turbulence timescale ($\approx \Omega^{-1}$). Using a smaller time step or grid spacing does not significantly change simulation results. The model parameters in LSM are specified as standard values listed in Table 1. However, the DCBL case simulation with $C_{\epsilon 3} = 0$ considerably underestimates mean dissipation because no dissipation is generated from turbulence production. Thus, we use $C_{\epsilon 3} = 0.72$ only for the DCBL case. For the DCBL and DCBL-S cases, all statistics shown in the following section are averages over ± 15 minutes of the selected time level. For the GABLS1 case, statistics are averages over the last simulation hour ($t = 8\text{--}9$ h).

5 Results

5.1 Dry Convective Boundary Layer (DCBL)

Figure 2 shows the vertical profiles of potential temperature, heat flux, and TKE in the simulations of the DCBL case at different time levels. LSM reproduces the gradual growth of the CBL and the formation of the inversion layer. The linear heat flux profile in the CBL and negative heat flux in the entrainment zone (region of negative heat flux) are simulated reasonably well in LSM, while the entrainment is slightly stronger in the LSM simulation. The magnitude of negative heat flux increases with time both in LES and LSM, consistent with the increasing inversion strength. Both models simulate negative heat flux peaks about 20% of surface heat flux at $t = 4$ h. The realistic simulation of the entrainment process in LSM without any explicit modeling is noticeable. Eddy-viscosity models need additional treatment of counter-gradient fluxes, and the entrainment in higher-order closure models is very sensitive to the parameterization of turbulent transport (e.g., Nakanishi and Niino 2009).

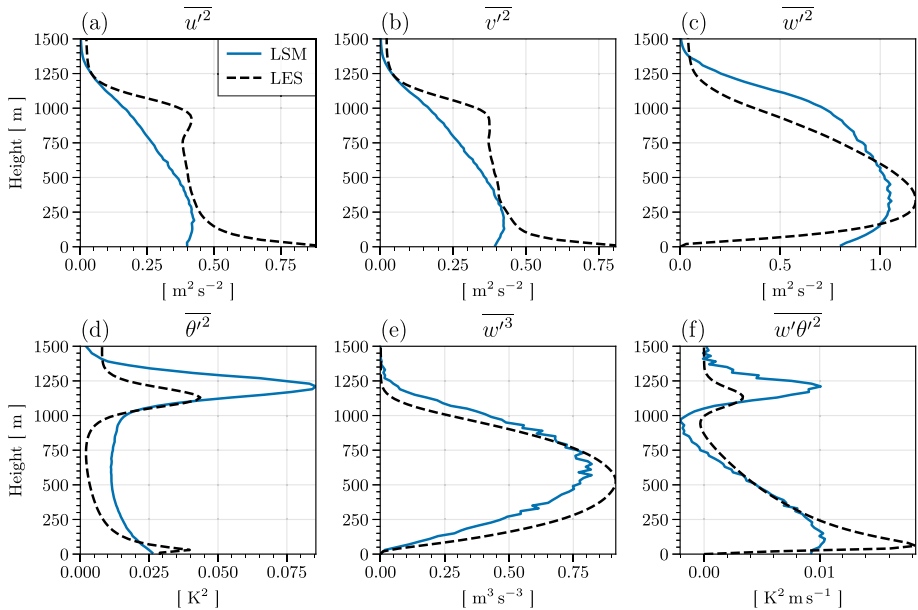


Fig. 3 Vertical profiles of various statistical moments in the simulations of the DCBL case from LSM (solid) and LES (dashed) at $t = 3$ h. The subgrid contributions are included in $\overline{u'^2}$, $\overline{v'^2}$, and $\overline{w'^2}$ for LES

The entrainment process in LSM is simulated very naturally in a Lagrangian framework, where the overshooting and mixing of air parcels into the inversion are all tracked.

The increase of TKE over time and the location of the maximum TKE (100–250 m) are similarly simulated in LES and LSM. However, LSM underestimates the vertical gradient of TKE near the inversion. This is related to the excessive TKE transport in the upper part of the entrainment zone. A detailed analysis, along with the TKE budget, will be discussed later. The one feature that LSM did not simulate well is the temperature gradient of the unstable layer at the near surface (Fig. 2a). We consider two explanations for this problem. One explanation is that it is due to the deficiency of the dissipation model. The unstable layer is mainly formed in the early stage of CBL development. The dissipation model of LSM does not work well when turbulence is initiated from zero turbulence. In (14), ω remains zero if ω and $\bar{\omega}$ are zero. The dissipation becomes non-zero only when the particles are reflected at the lower boundary. Therefore, the dissipation in the early stage of CBL is substantially underestimated, so strong turbulent mixing reduces the temperature gradient of the unstable layer. Another explanation is given in Fig. 4.

Figure 3 shows the vertical profiles of several statistical moments simulated by LES and LSM at $t = 3$ h. While the TKE profiles of LES and LSM are similar, the velocity variance components show noticeable differences between the two models. LSM overestimates (underestimates) $\overline{w'^2}$ ($\overline{u'^2}$ and $\overline{v'^2}$) near the surface and near the CBL top. In LES, near-surface turbulence is highly anisotropic in a way that the vertical component is damped and approaches zero at the surface boundary. The overestimation of $\overline{w'^2}$ in LSM implies that the parameterization of pressure redistribution has a deficiency near the surface. It should be noted that LES also uses some modeling assumptions near the surface. Therefore, it can be physically incorrect that the variance of the vertical velocity goes to zero in LES. The fluc-

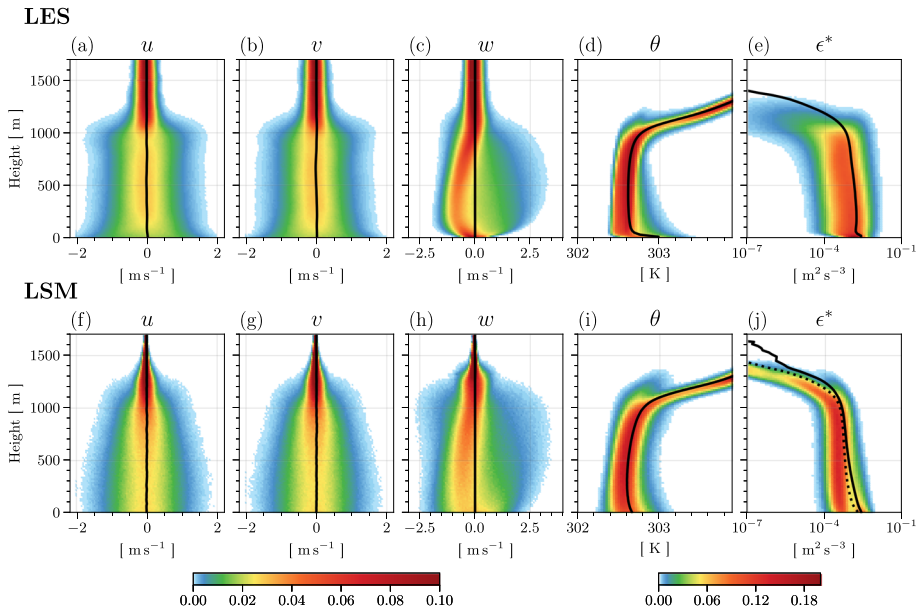


Fig. 4 Vertical distributions of the probability density of **a, f** u , **g, h** v , **c, h** w , **d, i** θ , and **e, j** local dissipation rate ϵ^* in the simulations of the DCBL case for LES (first row) and LSM (second row) at $t = 3$ h. At each level, the integration of probability density equals 1. The solid and dotted lines in **j** denote $\epsilon = \Omega k$ and $\overline{\omega k}$, respectively, and solid lines in other panels denote the mean profile

tuating pressure at the near surface is largely affected by the presence of a wall (Gibson and Launder 1978). The wall effect can be modeled either by damping functions (e.g., Hanjalic and Launder 1976,) or elliptic relaxation (Durbin 1991), which is a more advanced method. The elliptic relaxation is a good candidate for LSM, as it can be applied to LSM approaches as proposed by Dreeben and Pope (1998), and the elliptic relaxation for stratified flows has been proposed recently (Das 2020). The simulation of turbulence anisotropy near the CBL top also needs to be improved. One hypothesis is that the inversion layer acts like a wall, modifying the pressure redistribution.

LSM reproduces the general shape of $\overline{\theta'^2}$ profile but overestimates $\overline{\theta'^2}$ by about a factor of 2 (Fig. 3d). LES and LSM simulate the bell-shaped profile of $\overline{w'^3}$ with similar magnitudes. The realistic simulation of $\overline{w'^3}$ by LSM indicates that the turbulent transport of LSM is working as expected. $\overline{w'\theta'^2}$ contributes to the turbulent transport of $\overline{\theta'^2}$. The strong gradients of $\overline{w'\theta'^2}$ near inversion explain the peak of $\overline{\theta'^2}$ in the inversion, while LSM simulates larger gradients.

Figure 4 shows the vertical distributions of the probability density of several variables. The PDFs of LSM are directly obtained from Lagrangian samples. The PDFs of LES are computed using LES grid values, so only resolved variabilities are taken into account. Therefore, any quantitative analysis with the PDFs needs caution, although the subgrid contribution is relatively small. A noticeable feature of the DCBL case is the asymmetric distribution of vertical velocity (Fig. 4c, h). The distribution of w is skewed, where downdrafts are generally weaker than updrafts. LSM reproduces the asymmetric distribution of w . However, the detailed distribution of w differs from LES. As demonstrated earlier, the variance of w is

overestimated near the bottom and top of CBL. In addition, the downdrafts in LSM are more energetic than in LES. LSM simulates downdrafts that are stronger than -2 m s^{-1} , which are absent in LES. LSM still reproduces some important aspects of the w distribution; updrafts are strongest in the middle of CBL, and downdrafts accelerate from the top to the bottom of CBL. Both models simulate the symmetric and near-Gaussian distributions of u and v , but LSM simulates smaller variances of u and v near the bottom and top of CBL.

The PDFs of the potential temperature exhibit the convective overshooting in the inversion layer for both models (Fig. 4d, i). At 1100–1200 m heights, a bulge of air parcels originating from lower levels is observed. The convective overshooting of LSM is stronger and extends higher than LES. LES exhibits a strong unstable layer and highly skewed distribution near the surface, but LSM shows a less pronounced unstable layer and skewness. The boundary condition (26) indicates that particles are heated by surface heat flux after reflection. As the vertical velocities of the reflected particles in LSM are high, the heated particles have less time to be mixed with the environment. Therefore, the unstable layer is weakly developed in LSM due to stronger vertical mixing of temperature. In contrast, in LES, heated air parcels have a longer time to be mixed with the environment. Figure 4d shows that the temperature of heated air parcels rapidly decreases as they rise from the surface in LES. The PDFs of local dissipation rate ϵ^* are log-normally distributed for both models, showing intermittency of turbulence. ϵ^* of LES varies in a much wider range compared to LSM, but it should be noted that the dissipation in LES is highly parameterized. The Smagorinsky–Lilly subgrid model in LES does not account for backscatter, so there is a possibility that the variance of dissipation is underestimated in LES.

Figure 5 shows the joint PDFs of vertical velocity and potential temperature at different heights. In general, LSM well reproduces the shapes of the joint PDFs simulated by LES. The joint PDFs are highly skewed and exhibit a curved shape for the positive velocity region. The curved-shape distributions are commonly observed in joint PDFs of turbulence and cloud properties (Bogenschütz et al. 2010; Chinita et al. 2018). However, they are not easy to be represented by assumed PDF methods, while double Gaussian can make an approximation. In the entrainment zone ($z = 1000 \text{ m}$), the joint PDF is separated into two regimes: negatively buoyant updrafts and compensating subsidence. LSM simulates the complex shape of joint PDF in the entrainment zone reasonably well. Nevertheless, some differences against LES are observed, where LSM simulates larger variances of w and θ in the negative velocity region for all heights and also simulates too strong updrafts and downdrafts in the entrainment zone.

Figure 6 shows the vertical profiles of TKE budget terms simulated by LES and LSM. The balance of buoyancy production, transport, and dissipation is similarly simulated in the two models. The negative and positive turbulent transports (T_i) in the lower and upper CBL, respectively, are reproduced in LSM. LSM simulates smaller negative T_i near the surface because vertical gradients of vertical velocities are underestimated in LSM. The turbulent transport of LSM in the upper entrainment zone is stronger than LES, so TKE in the inversion layer is greater than LES (Fig. 2c). The pressure transport is explicitly modeled in the LSM equations, playing a role in compensating turbulent transport. The pressure transport term T_p simulated in LSM is substantially smaller than in LES. The dissipation of TKE is also generally underestimated in LSM. The pressure transport and dissipation largely affect simulation results, and they can be controlled by changing model parameters. The control of these processes will be discussed in Sect. 6.1. The residuals of the TKE budgets are not zero in LES and LSM, where the residual of LES is notably larger. The residuals are expected to result from statistical errors in computing TKE budget terms. The budgets do not add up to exactly zero as the budgets are computed from a limited number of samples.

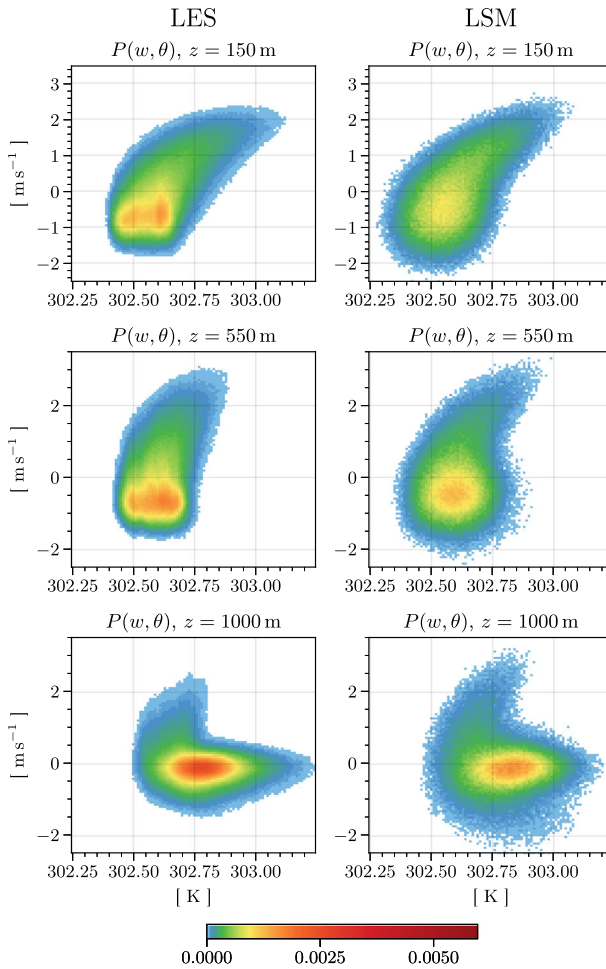


Fig. 5 Joint PDFs of vertical velocity and potential temperature in the simulations of the DCBL case from LES (first column) and LSM (second column) at the heights of 150, 550, and 1000 m at $t = 3$ h

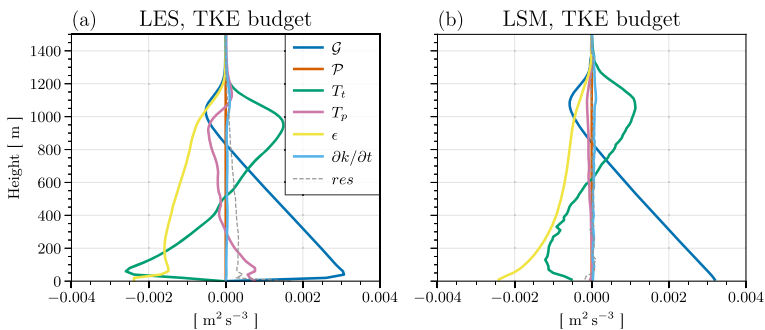


Fig. 6 Vertical profiles of TKE budget terms in the simulations of the DCBL case from **a** LES and **b** LSM at $t = 3$ h. res is the residual of the TKE budget calculation. The subgrid contributions to the budget terms are included in LES

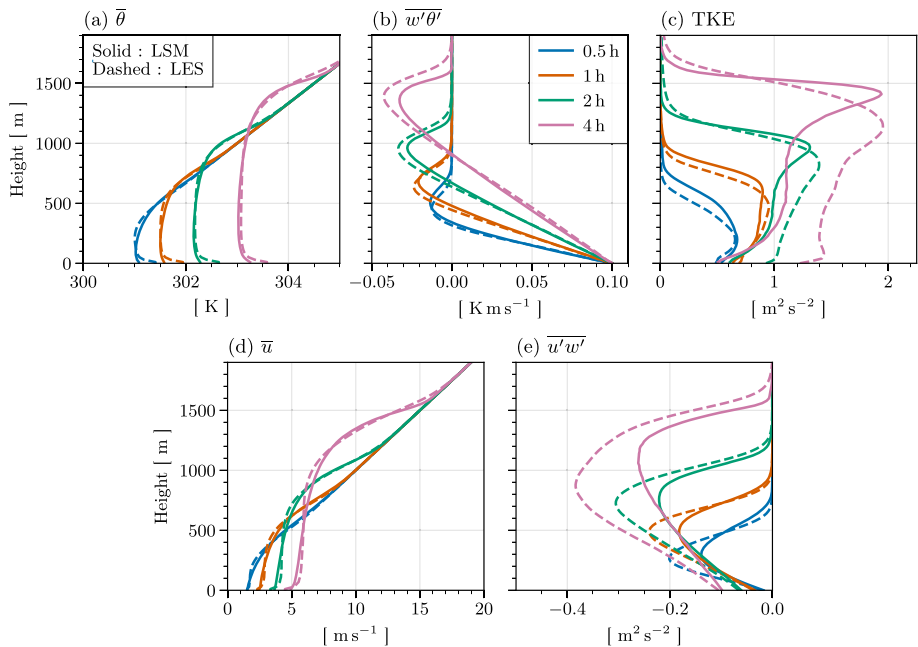


Fig. 7 Vertical profiles of **a** $\bar{\theta}$, **b** $\overline{w'\theta'}$, **c** TKE, **d** \bar{u} , and **e** $\overline{u'w'}$ in the simulations of the DCBL-S case from LSM (solid) and LES (dashed) at $t = 0.5, 1, 2$, and 4 h

5.2 Dry Convective Boundary Layer with Shear (DCBL-S)

Figure 7 shows the vertical profiles of several statistics in the simulations of the DCBL-S case. The gradual growth of CBL and the formation of the inversion layer are simulated similarly to the DCBL case. The zonal wind profiles also exhibit the growth of the mixing and inversion layer (Fig. 7d). The entrainment zone and inversion layer of the DCBL-S case are substantially deeper than the DCBL case. The entrainment of CBL is enhanced by vertical wind shear (Moeng and Sullivan 1994; Kim et al. 2003), and the enhancement of entrainment is determined by the fraction of shear-generated TKE that contributes to the entrainment process (Conzemius and Fedorovich 2006). LSM also simulates a deeper entrainment zone and inversion layer compared to the DCBL case, while the entrainment is slightly weaker than LES. The enhancement of entrainment in LSM is partially due to the change in the value of $C_{\epsilon 3}$ from 0.72 to 0. If the same value of $C_{\epsilon 3} = 0$ is used for the two cases, LSM still simulates enhanced entrainment by shear production but to a smaller extent. Compared to LES, LSM simulates slightly more stable stratification and stronger wind gradient in the mixing layer. The temperature and wind gradients in the unstable layer are underestimated, similar to the DCBL case, probably due to a large vertical velocity variance near the surface.

The simulated profiles of TKE are top-heavy as the shear production is strong near the entrainment zone (Fig. 7c). LSM simulates an increase of TKE in the upper CBL but fails to reproduce an increase of TKE in the lower CBL. This is because the shear production is underestimated near the surface (Fig. 8), as the wind gradient is weakly simulated in LSM. The two models calculate similar momentum fluxes near the surface, but LSM substantially underestimates momentum fluxes at upper levels (Fig. 7e). The momentum flux can be enhanced if more momentum of the free atmosphere is entrained into the CBL.

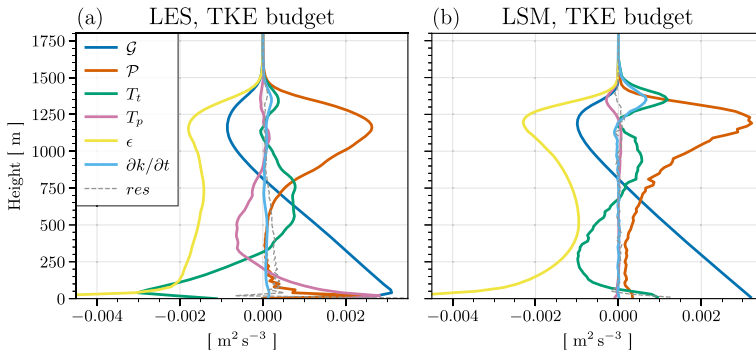


Fig. 8 Vertical profiles of TKE budget terms in the simulations of the DCBL-S case from **a** LES and **b** LSM at $t = 3$ h. *res* is the residual of the TKE budget calculation. The subgrid contributions to the budget terms are included in LES

The TKE budget of the DCBL-S case (Fig. 8) is much more complex than the non-sheared case. In the entrainment zone, the turbulent transport is considerably smaller than in the DCBL case. This is because the upward transport of buoyancy-generated TKE is offset by the downward transport of shear-generated TKE (Conzemius and Fedorovich 2006). The turbulent transport shows a bimodal profile in the entrainment zone, indicating that the shear-generated TKE is transported upward and downward and consequently deepens the entrainment zone. LSM reproduces the relatively small and bimodal turbulent transport in the entrainment zone. However, LSM simulates too strong turbulent transport and time tendency of TKE in the upper part of the entrainment zone. In LES, TKE is strongly transported downward in the CBL by pressure transport, but LSM lacks pressure transport in the CBL. In the sheared CBL, the interaction of updrafts/downdrafts and vortical structures can generate strong pressure transport (Lin 2000). Unfortunately, this kind of pressure fluctuation is hard to be modeled with Reynolds stress modeling approaches. The profile of dissipation in LSM is somewhat more top-heavy compared to that in LES, as TKE is more top-heavy in LSM.

5.3 Stably Stratified Atmospheric Boundary Layer (GABLS1)

A stable ABL (SABL) is a case in which turbulence models are difficult to simulate. The result of GABLS1 intercomparison of turbulence closure models demonstrated large variations among models and overpredicted mixing (Cuxart et al. 2006). Figure 9 shows the vertical profiles of some statistics in the simulations of the GABLS1 case. The results from the LES intercomparison of the GABLS1 case (Beare et al. 2006) are also plotted. LSM simulates realistic mixing intensity (Fig. 9e), and the simulated statistics are comparable to that of LES. LSM also reproduces the low-level jet and wind-turning effect (Fig. 9b, c). The height of the SABL in LSM is similar to UCLA-LES but slightly lower than the LES ensemble mean. LSM simulates a larger gradient of $\bar{\theta}$ and a sharper lower-level jet profile near the SABL top, which may indicate a weaker mixing with the free atmosphere.

The profiles of gradient Richardson numbers are plotted to see whether turbulent fluxes in LSM have correct Richardson number dependency (Fig. 9d). In the LES ensemble, the Richardson numbers in the SABL are measured in the range from 0 to the critical Richardson number of about $Ri_c \approx 0.25$, and TKE becomes zero when $Ri \rightarrow Ri_c$. UCLA-LES exhibits high Ri in the SABL, largely deviating from the LES ensemble. The Ri profile of LSM

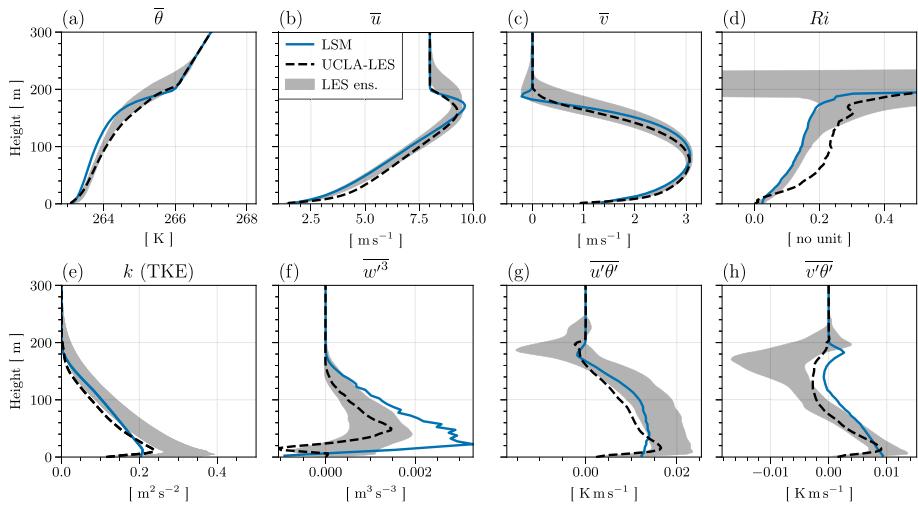


Fig. 9 Vertical profiles of **a** $\bar{\theta}$, **b** \bar{u} , **c** \bar{v} , **d** gradient Richardson number Ri , **e** TKE, **f** $\overline{w'^3}$, **g** $\overline{u'\theta'}$, and **h** $\overline{v'\theta'}$ in the simulations of the GABLS1 case from LSM (solid), UCLA-LES (dashed), and LES ensemble (shaded) averaged over $t = 8\text{--}9$ h. The shade denotes one standard deviation range of LES ensemble members from Beare et al. (2006)

is relatively well matched with the LES ensemble profiles and shows a critical Richardson number of about $Ri_c \approx 0.2$. The magnitude of $\overline{w'^3}$ (and skewness of w) is small in GABLS1 as turbulent transport is not important as in the CBL. LSM overpredicts $\overline{w'^3}$ about a factor of 2. Unlike eddy viscosity models, Reynolds stress models have the ability to simulate horizontal heat fluxes as well as vertical heat flux. LSM predicts horizontal heat fluxes reasonably (Fig. 9g, h), but due to weaker mixing with the free atmosphere, the negative $\overline{v'\theta'}$ in the upper SABL in the LES ensemble is not predicted in LSM.

LSM well reproduces the PDF of the GABLS1 case simulated in LES (Fig. 10). The turbulence statistics are close to Gaussian in the GABLS1 case, so there are no additional merits for using LSM over SMC models. However, it is noticeable that LSM shows comparable performance to sophisticated Reynolds stress models in the simulation of SABL (e.g., Želi et al. 2020). LSM predicts symmetric Gaussian distributions with similar variances as LES. The simulated variances of velocity components and temperature decrease with height, according to the decreasing TKE with height. The notable deficiency of LSM is the overestimated vertical velocity variance near the surface and the slight overestimation of temperature variance.

The TKE budget of the GABLS1 case (Fig. 11) shows that transport terms are very small compared to production and dissipation terms. The shear production, buoyancy production, and dissipation are in balance, where the magnitude of buoyancy production is relatively small. LSM accurately reproduces the budget balance. Due to the balance, the simulation of GABLS1 is highly sensitive to the modeling of dissipation. Želi et al. (2020), who adopted a $k\text{--}\epsilon$ based dissipation model to simulate the GABLS1 case, demonstrated that the model performance increases when the parameters in the dissipation model ($C_{\epsilon 2}$ and $C_{\epsilon 3}$) are parameterized as a function of stability.

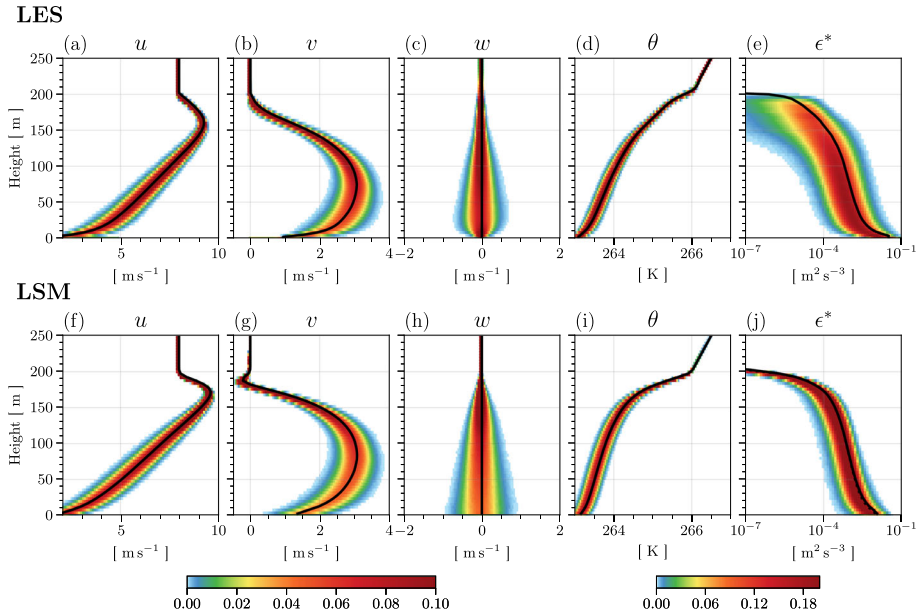


Fig. 10 Vertical distributions of the probability density of **a, f** u , **b, g** v , **c, h** w , **d, i** θ , and **e, j** local dissipation rate ϵ^* in the simulations of the GABLS1 case from LES (first row) and LSM (second row) averaged over $t = 8-9$ h. At each level, the integration of probability density equals 1. The solid and dotted lines in **j** denote $\epsilon = \Omega k$ and $\overline{\omega} k$, respectively, and solid lines in other panels denote the mean profile

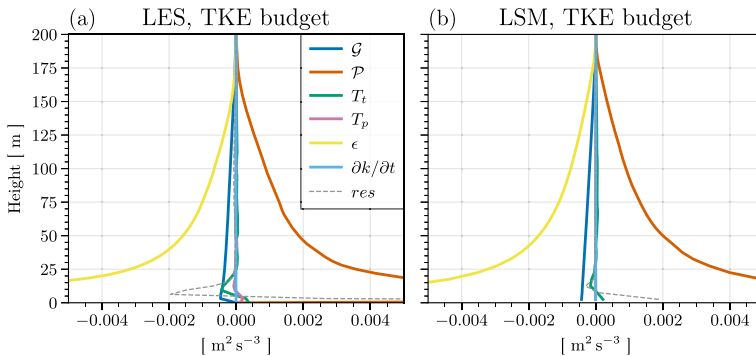


Fig. 11 Vertical profiles of TKE budget terms in the simulations of the GABLS1 case from **a** LES and **b** LSM averaged over $t = 8-9$ h. *res* is the residual of the TKE budget calculation. The subgrid contributions to the budget terms are included in LES

6 Discussion

6.1 Sensitivity to Model Parameters

The simulation results suggest that the model performance is sensitive to the parameterization of dissipation and pressure transport. In the dissipation model of (14) and (15), the buoyancy effect is the largest source of uncertainty. In this section, LSM simulations with different values of $C_{\epsilon 3}$ and C_{pt} , which control the buoyancy-generated dissipation and pres-

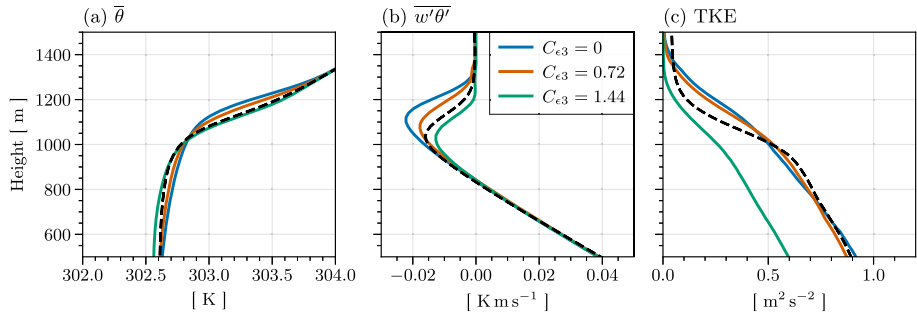
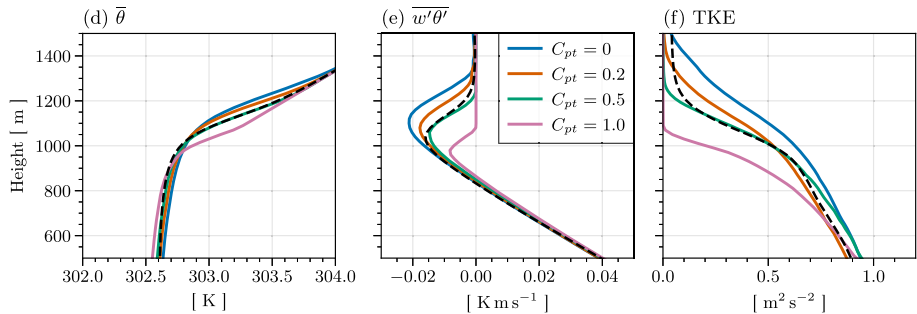
Sensitivity test : $C_{\epsilon 3}$ Sensitivity test : C_{pt} 

Fig. 12 Vertical profiles of the LSM simulations of the DCBL case with different values of (first row) $C_{\epsilon 3}$ and (second row) C_{pt} at $t = 3$ h. The dashed line denotes the profile from LES

sure transport, respectively, are tested. Figure 12 shows the result of the sensitivity test for the DCBL case. As the value of $C_{\epsilon 3}$ increases, the entrainment gets weaker because the dissipation in the CBL is enhanced. The potential temperature and heat flux profiles indicate that the optimal value of $C_{\epsilon 3}$ is between 0.72 and 1.44. However, if $C_{\epsilon 3}$ is larger than 0.72, TKE is considerably underestimated in the CBL due to strong dissipation. C_{pt} controls the strength of entrainment too, but in a different way than $C_{\epsilon 3}$ does. C_{pt} does not change TKE in the CBL but changes the gradient of TKE in the inversion layer. The pressure transport effectively controls convective overshooting as it exerts a force on high-energy particles in the direction of the TKE gradient. The LSM with $C_{pt} = 0.5$ simulates profiles that match the LES profiles very well, with a realistic TKE gradient in the inversion layer.

6.2 Computational Cost and Bias Error

The computational cost of PDF methods is in between LES and turbulence closure models (Pope 2000). The computational cost of LSM is evaluated in the simulations of the DCBL case with different total particle numbers N_p . The code of LSM is written in the Julia programming language (Bezanson et al. 2017), and the simulations are executed in a single core of 2.9GHz Intel Xeon CPU. The simulation execution time increases almost linearly with N_p (Fig. 13a). The 4-hour DCBL case simulation takes 564s for $N_p = 200000$ and 113s for $N_p = 50000$. It is important to choose appropriate N_p so that the computational cost is not too high and errors of simulated statistics are small. Figure 13b shows the heat

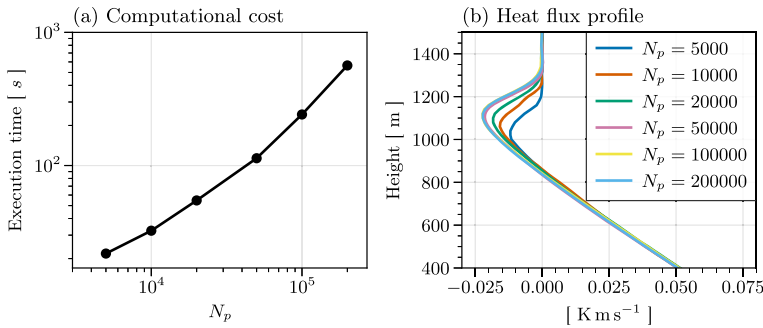


Fig. 13 **a** Execution time as a function of total particle number N_p from the LSM simulations of the DCBL case. The simulations are integrated for 4 simulation hours (2880 time steps). **b** Heat flux profiles of the DCBL case at $t = 3$ h, simulated by LSM with different N_p

flux profiles of the simulations with different N_p . The simulation results almost converge when $N_p > 50000$. The simulations with smaller N_p have systematic biases with reduced entrainment. Similar particle methods are known to have error scaling of N_p^{-1} for bias error and $N_p^{-1/2}$ for statistical error (random fluctuations in turbulence statistics) (Pope 1995; Jenny et al. 2001).

Proper variance reduction techniques can significantly reduce biases and statistical errors of LSM. As a result, a smaller particle number can be used, and computational cost can be reduced. Popular variance reduction techniques for Monte Carlo simulation, such as importance sampling and control variate, can be adopted. The importance sampling can be used to remove particles that have a small impact on the turbulent flux by preferentially sampling particles with high vertical velocities. The temporal averaging of turbulence statistics can also be used to reduce biases and statistical errors. One idea is to use different time steps for particle evolution and turbulence statistics evaluation. For example, if particle evolution is integrated with $\Delta t_{\text{sub}} = 2$ s and turbulence statistics are evaluated with $\Delta t = 2$ min, then 60 times more samples are available for Reynolds averaging. In this case, the Reynolds averaging operator becomes the horizontal and temporal average for 2 min. We expect that using a larger time step as a mesoscale or larger-scale atmospheric model with a smaller particle number is possible with this technique.

7 Summary and Conclusions

Due to the moment closure assumption, atmospheric turbulence closure models provide information on turbulence statistics only for several orders of moments. In this study, we propose a single-column turbulence model, which solves the transport equations of turbulence PDF using a Lagrangian stochastic modeling (LSM) approach. The stochastic differential equations (SDEs) for particle velocity and temperature suggested by Das and Durbin (2005) are adopted, which exactly reproduce the second-moment transport equations that are widely used to model stratified ABL. To extend the LSM of Das and Durbin (2005) to inhomogeneous turbulence, a simple parameterization of pressure transport is included in the SDEs. In addition, an SDE for dissipation is adopted, which is designed for inhomogeneous turbulence and based on the k - ϵ model. In the proposed model, the properties and positions of particles are evolved along SDEs, and the turbulence statistics are calculated as the ensemble mean

of particles. Then, the time evolution of a mean field is calculated as the convergence of turbulent flux. The model provides a full representation of turbulence PDF and simulates turbulent transport without any modeling assumption. The model performance is evaluated against LES results in the simulations of three idealized cases: the DCBL, DCBL with shear (DCBL-S), and GABLS1 cases.

In the DCBL case, LSM simulates the gradual growth of the CBL, and the simulated potential temperature, heat flux, and TKE profiles are in good agreement with the LES profiles. Particularly, LSM simulates a realistic entrainment process by tracking of Lagrangian particles, so the shape and magnitude of the time-dependent negative heat flux profile in the entrainment zone are well simulated. A deficiency of LSM is the weak temperature gradient in the near-surface unstable layer. This is likely due to the weak dissipation in the early stage of CBL development and too large vertical velocity variance near the surface. LSM overestimates (underestimates) vertical (horizontal) velocity variance near the bottom and top of the CBL. The result implies that the current model needs to be improved to include the wall effect, which accounts for the modification of pressure redistribution near the wall. Both LSM and LES simulate a bell-shaped profile of triple moment of vertical velocity with similar magnitudes, indicating that LSM simulates turbulent transport in a realistic way.

The PDF simulated by LSM reveals a detailed depiction of the CBL structure. LSM reproduces the asymmetric distribution of vertical velocity and the separation of temperature distribution by convective overshooting. LSM also reproduces the curved and highly skewed shape of the joint PDF of vertical velocity and potential temperature. In the entrainment zone, the joint PDF is separated into two regimes with a complex shape, and LSM successfully reproduces the shape of the joint PDF. However, the PDF of LSM exhibits errors in temperature variance and turbulence anisotropy. LSM with standard model parameters slightly overestimates the magnitude of entrainment in the DCBL case because downward pressure transport is underestimated. The magnitude of entrainment can be effectively controlled by changing the model parameter related to pressure transport.

The DCBL-S case exhibits a deeper entrainment zone than the DCBL case because a fraction of shear production contributes to the entrainment process. LSM partially reproduces the enhancement of entrainment by shear production. A TKE budget reveals that LSM can simulate the modification of turbulent transport by shear but also reveals problems of LSM in simulating shear production near the surface and pressure transport in the sheared CBL. In the GABLS1 case, LSM is able to predict realistic mean and flux profiles along with distinct features of the SABL, such as low-level jets and wind turning. The critical Richardson number of LSM is measured as ≈ 0.2 . The transport terms are relatively small in the SABL, so the PDF is close to Gaussian. LSM reproduces the Gaussian PDF with comparable variances, but the vertical velocity variance near the surface is overestimated.

In this study, LSM is tested with minimal modifications and with standard model parameters. LSM provides a full representation of turbulence PDF while having reasonable performance in predicting mean fields. Some well-developed or well-calibrated turbulence closure models (e.g., Nakanishi and Niino 2009) may produce better predictions on mean fields and moments (not tested yet). The performance of LSM can be significantly improved through calibrating parameters and better modeling of the pressure transport, wall effect on pressure redistribution, and dissipation. In that case, LSM can be served as a tool to evaluate higher-order closure models.

Most mesoscale and global atmospheric models calculate physics tendencies in each atmospheric column, so the proposed LSM can be implemented in these models as a subgrid turbulence parameterization. The computational cost of LSM is much larger than that of turbulence closure models, so the use of LSM in 3D atmospheric models is currently limited.

However, as previously discussed, the computational cost of LSM can be managed by various variance reduction techniques, allowing the use of fewer particles by reducing biases and statistical errors. A good example is the Monte Carlo radiative transfer modeling, which successfully reduces its computational cost using variance reduction techniques (Räsänen and Barker 2004; Iwabuchi 2006). LSM has the benefit that the dispersion of passive scalars can be computed natively inside LSM. Moreover, LSM can be extended to simulate subgrid moist turbulence and convection in a unified framework when it is coupled with microphysics. The use of turbulence and convection schemes in an atmospheric model implies the separation of subgrid vertical transport by the two schemes. However, the separation is not precisely defined, resulting in missing or double-counted vertical transport. In LSM, every transport is Lagrangian, so local and non-local mixing can not be distinguished. One can notice that the LSM equations are similar to the transport equations in convection schemes and the turbulence frequency ($\omega = \epsilon/k$) is closely related to the convective entrainment rate. A stochastic parameterization of the convection mixing process will allow a realistic simulation of the variability of convective clouds (e.g., Shin and Baik 2022). In the near future, simulation results for various cloud types with the LSM approach will be reported.

Acknowledgements The authors are grateful to three anonymous reviewers for providing valuable comments on this work. This work was supported by the National Research Foundation of Korea (NRF) grant funded by the Korea government (MSIT) (No. RS-2023-00214037).

Funding Open Access funding enabled and organized by Seoul National University.

Open Access This article is licensed under a Creative Commons Attribution 4.0 International License, which permits use, sharing, adaptation, distribution and reproduction in any medium or format, as long as you give appropriate credit to the original author(s) and the source, provide a link to the Creative Commons licence, and indicate if changes were made. The images or other third party material in this article are included in the article's Creative Commons licence, unless indicated otherwise in a credit line to the material. If material is not included in the article's Creative Commons licence and your intended use is not permitted by statutory regulation or exceeds the permitted use, you will need to obtain permission directly from the copyright holder. To view a copy of this licence, visit <http://creativecommons.org/licenses/by/4.0/>.

Appendix 1

The particle density correction algorithm from Wild (2013) is adopted so that the time-averaged particle density is consistent with the basic state density ρ_0 . The particle density \bar{q} at the grid midpoint z_k is calculated as:

$$\begin{aligned} m^* &= \left(\int_z \rho_0 dz \right) / N_p, \\ (\bar{q})_k &= \frac{m^* \sum_{n=1}^{N_p} (\hat{g}_k(z^*))_n}{z_{k+\frac{1}{2}} - z_{k-\frac{1}{2}}}, \end{aligned} \quad (33)$$

where m^* is the mass per unit area (kg m^{-2}) of a particle. To reduce statistical fluctuation on \bar{q} , the following time-averaging technique is used,

$$\begin{aligned} \bar{q}_{\text{avg}}^{n+1} &= \mu \bar{q}_{\text{avg}}^n + (1 - \mu) \bar{q}^{n+1}, \\ \mu &= \frac{K - 1}{K}, \quad K \geq 1, \end{aligned} \quad (34)$$

where \bar{q}_{avg}^n is the time-averaged \bar{q} at the time level of n and K is the time-averaging factor. $K = 100$ is used for this study.

The normalized density error Q is defined using the time-averaged particle density:

$$Q = \frac{\bar{q}_{\text{avg}} - \rho_0}{\rho_0}. \quad (35)$$

The correction velocity w^c is computed as:

$$w^c = -a \frac{\partial Q}{\partial z},$$

$$a = C_{\text{pos}} \min \left(\frac{(\text{CFL})_p^c \Delta z}{\left\| \frac{\partial Q}{\partial z} \right\| \Delta t} \right) \tanh(10 \max(Q)), \quad (36)$$

where C_{pos} and $(\text{CFL})_p^c$ are parameters and are specified as 0.2 and 0.5, respectively. The correction velocity is added to the particle velocity to update the particle position. The correction velocity is typically very small ($|w^c| < 0.05 \text{ m s}^{-1}$) compared to the particle velocity.

References

- Beare RJ, Macvean MK, Holtslag AAM, Cuxart J, Esau I, Golaz JC, Jimenez MA, Khairoutdinov M, Kosovic B, Lewellen D, Lund TS, Lundquist JK, McCabe A, Moene AF, Noh Y, Raasch S, Sullivan P (2006) An intercomparison of large-eddy simulations of the stable boundary layer. *Boundary-Layer Meteorol* 118:247–272
- Bezanson J, Edelman A, Karpinski S, Shah VB (2017) Julia: a fresh approach to numerical computing. *SIAM Rev* 59(1):65–98
- Bogenschutz PA, Krueger SK, Khairoutdinov M (2010) Assumed probability density functions for shallow and deep convection. *J Adv Model Earth Syst* 2(4)
- Bogenschutz PA, Gettelman A, Morrison H, Larson VE, Craig C, Schanen DP (2013) Higher-order turbulence closure and its impact on climate simulations in the Community Atmosphere Model. *J Clim* 26(23):9655–9676
- Businger JA, Wyngaard JC, Izumi Y, Bradley EF (1971) Flux-profile relationships in the atmospheric surface layer. *J Atmos Sci* 28(2):181–189
- Chinita MJ, Matheou G, Teixeira J (2018) A joint probability density-based decomposition of turbulence in the atmospheric boundary layer. *Mon Weather Rev* 146(2):503–523
- Conzemius RJ, Fedorovich E (2006) Dynamics of sheared convective boundary layer entrainment. Part I: methodological background and large-eddy simulations. *J Atmos Sci* 63(4):1151–1178
- Cuxart J, Holtslag AAM, Beare RJ, Bazile E, Beljaars A, Cheng A, Conangla L, Ek M, Freedman F, Hamdi R, Kerstein A, Kitagawa H, Lenderink G, Lewellen D, Mailhot J, Mauritsen T, Perov V, Schayes G, Steeneveld GJ, Svensson G, Taylor P, Weng W, Wunsch S, Xu KM (2006) Single-column model intercomparison for a stably stratified atmospheric boundary layer. *Boundary-Layer Meteorol* 118:273–303
- Danabasoglu G, Lamarque JF, Bacmeister J, Bailey DA, Du Vivier AK, Edwards J, Emmons LK, Fasullo J, Garcia R, Gettelman A, Hannay C, Holland MM, Large WG, Lauritzen PH, Lawrence DM, Lenaerts JTM, Lindsay K, Lipscomb WH, Mills MJ, Neale R, Oleson KW, Otto-Bliesner B, Phillips AS, Sacks W, Tilmes S, van Kampenhout L, Vertenstein M, Bertini A, Dennis J, Deser C, Fischer C, Fox-Kemper B, Kay JE, Kinnison D, Kushner PJ, Larson VE, Long MC, Mickelson S, Moore JK, Nienhouse E, Polvani L, Rasch PJ, Strand WG (2020) The community earth system model version 2 (CESM2). *J Adv Model Earth Syst* 12(2):e2019MS001916
- Das SK (2020) A Reynolds Stress model with a new elliptic relaxation procedure for stratified flows. *Int J Heat Fluid Flow* 83:108595
- Das SK, Durbin PA (2005) A Lagrangian stochastic model for dispersion in stratified turbulence. *Phys Fluids* 17(2):025109
- Dreeben TD, Pope SB (1997) Wall-function treatment in pdf methods for turbulent flows. *Phys Fluids* 9(9):2692–2703

- Dreeben TD, Pope SB (1998) Probability density function/Monte Carlo simulation of near-wall turbulent flows. *J Fluid Mech* 357:141–166
- Durbin PA (1991) Near-wall turbulence closure modeling without “damping functions”. *Theor Comput Fluid Dyn* 3(1):1–13
- Dyer A (1974) A review of flux-profile relationships. *Boundary-Layer Meteorol* 7:363–372
- Fitch AC (2019) An improved double-Gaussian closure for the subgrid vertical velocity probability distribution function. *J Atmos Sci* 76(1):285–304
- Gibson M, Launder B (1978) Ground effects on pressure fluctuations in the atmospheric boundary layer. *J Fluid Mech* 86(3):491–511
- Golaz JC, Larson VE, Cotton WR (2002) A pdf-based model for boundary layer clouds. Part I: method and model description. *J Atmos Sci* 59(24):3540–3551
- Goudsmit GH, Burchard H, Peeters F, Wüest A (2002) Application of k-epsilon turbulence models to enclosed basins: the role of internal seiches. *J Geophys Res: Oceans* 107(C12):23-1–23-13
- Hanjalić K, Launder BE (1976) Contribution towards a Reynolds-stress closure for low-Reynolds-number turbulence. *J Fluid Mech* 74(4):593–610
- Heinz S (1997) Nonlinear Lagrangian equations for turbulent motion and buoyancy in inhomogeneous flows. *Phys Fluids* 9(3):703–716
- Iwabuchi H (2006) Efficient Monte Carlo methods for radiative transfer modeling. *J Atmos Sci* 63(9):2324–2339
- Jenny P, Pope SB, Muradoglu M, Caughey DA (2001) A hybrid algorithm for the joint PDF equation of turbulent reactive flows. *J Comput Phys* 166(2):218–252
- Kim SW, Park SU, Moeng CH (2003) Entrainment processes in the convective boundary layer with varying wind shear. *Boundary-Layer Meteorol* 108:221–245
- Kolmogorov AN (1962) A refinement of previous hypotheses concerning the local structure of turbulence in a viscous incompressible fluid at high Reynolds number. *J Fluid Mech* 13(1):82–85
- Launder BE, Reece GJ, Rodi W (1975) Progress in the development of a Reynolds-stress turbulence closure. *J Fluid Mech* 68(3):537–566
- Li T, Wang M, Guo Z, Yang B, Xu Y, Han X, Sun J (2022) An updated CLUBB PDF closure scheme to improve low cloud simulation in CAM6. *J Adv Model Earth Syst* 14(12):e2022MS003127
- Lin CL (2000) Local pressure-transport structure in a convective atmospheric boundary layer. *Phys Fluids* 12(5):1112–1128
- Moeng CH, Sullivan PP (1994) A comparison of shear-and buoyancy-driven planetary boundary layer flows. *J Atmos Sci* 51(7):999–1022
- Muradoglu M, Pope SB, Caughey DA (2001) The hybrid method for the PDF equations of turbulent reactive flows: consistency conditions and correction algorithms. *J Comput Phys* 172(2):841–878
- Nakanishi M, Niino H (2009) Development of an improved turbulence closure model for the atmospheric boundary layer. *J Meteorol Soc Jpn Ser II* 87(5):895–912
- Pearson HJ, Puttock JS, Hunt JCR (1983) A statistical model of fluid-element motions and vertical diffusion in a homogeneous stratified turbulent flow. *J Fluid Mech* 129:219–249
- Pereira J, Rocha J (2010) Prediction of stably stratified homogeneous shear flows with second-order turbulence models. *Fluid Dyn Res* 42(4):045509
- Pope SB (1983) A Lagrangian two-time probability density function equation for inhomogeneous turbulent flows. *Phys Fluids* 26(12):3448–3450
- Pope SB (1994) On the relationship between stochastic Lagrangian models of turbulence and second-moment closures. *Phys Fluids* 6(2):973–985
- Pope SB (1995) Particle method for turbulent flows: integration of stochastic model equations. *J Comput Phys* 117(2):332–349
- Pope SB (2000) *Turbulent flows*. Cambridge University Press
- Räisänen P, Barker HW (2004) Evaluation and optimization of sampling errors for the Monte Carlo Independent Column Approximation. *Q J R Meteorol Soc* 130(601):2069–2085
- Schmüdgen K (2017) *The moment problem*, vol 9. Springer
- Shin J, Baik JJ (2022) Parameterization of stochastically entraining convection using machine learning technique. *J Adv Model Earth Syst* 14(5):e2021MS002817
- Stevens B, Moeng CH, Sullivan PP (1999) Large-eddy simulations of radiatively driven convection: sensitivities to the representation of small scales. *J Atmos Sci* 56(23):3963–3984
- Stevens B, Moeng CH, Ackerman AS, Bretherton CS, Chlond A, de Roode S, Edwards J, Golaz JC, Jiang H, Khairoutdinov M, Kirkpatrick MP, Lewellen DC, Lock A, Müller F, Stevens DE, Whelan E, Zhu P (2005) Evaluation of large-eddy simulations via observations of nocturnal marine stratocumulus. *Mon Weather Rev* 133(6):1443–1462
- Taylor GI (1922) Diffusion by continuous movements. *Proc Lond Math Soc* 2(1):196–212

- Thomson DJ (1987) Criteria for the selection of stochastic models of particle trajectories in turbulent flows. *J Fluid Mech* 180:529–556
- Van Slooten PR, Jayesh, Pope SB (1998) Advances in PDF modeling for inhomogeneous turbulent flows. *Phys Fluids* 10(1):246–265
- Venayagamoorthy S, Koseff J, Ferziger J, Shih L (2003) Testing of RANS turbulence models for stratified flows based on DNS data. Center for Turbulence Research annual research briefs 2003
- Venkatram A, Strimaitis D, Dicristofaro D (1984) A semiempirical model to estimate vertical dispersion of elevated releases in the stable boundary layer. *Atmos Environ* 18(5):923–928
- Wild MA (2013) General purpose PDF solution algorithm for reactive flow simulations in OpenFOAM. PhD thesis, ETH Zurich
- Želi V, Brethouwer G, Wallin S, Johansson AV (2020) Modelling of stably stratified atmospheric boundary layers with varying stratifications. *Boundary-Layer Meteorol* 176(2):229–249

Publisher's Note Springer Nature remains neutral with regard to jurisdictional claims in published maps and institutional affiliations.